Received: 12 October 2023 | Revised: 18 January 2024 | Accepted: 23 January 2024

DOI: 10.1111/jace.19749

Journal of American Ceramic Society

RESEARCH ARTICLE

A quantitative microscopic view on the gas-phase-dependent phase transformation from tetragonal to monoclinic ZrO_2

Maged F. Bekheet[1] | **Lukas Schlicker**[1] | **Radian Popescu**[2] | **Wiebke Riedel**[3] | **Matthias Grünbacher**[4] | **Simon Penner**[4] | **Aleksander Gurlo**[1]

[1]Technische Universität Berlin, Faculty III Process Sciences, Institute of Materials Science and Technology, Chair of Advanced Ceramic Materials, Berlin, Germany

[2]Karlsruher Institut für Technologie (KIT), Laboratorium für Elektronenmikroskopie, Kaiserstrasse 12, Karlsruhe, Germany

[3]Institut für Chemie, Freie Universität Berlin, Berlin, Germany

[4]Institute of Physical Chemistry, University of Innsbruck, Innsbruck, Austria

Correspondence
Maged F. Bekheet, Technische Universität Berlin, Faculty III Process Sciences, Institute of Materials Science and Technology, Chair of Advanced Ceramic Materials, Straße des 17. Juni 135, 10623 Berlin, Germany.
Email: maged.bekheet@ceramics.tu-berlin.de

Present address
Lukas Schlicker, FACTUREE der Online-Fertiger, Berlin, Germany

Funding information
FWF (Austrian Science Foundation), Grant/Award Number: F4503-N16; Deutsche Forschungsgemeinschaft (DFG)

Abstract

ZrO_2 is a versatile material with diverse applications, including structural ceramics, sensors, and catalysts. The properties of ZrO_2 are largely determined by its crystal structure, which is temperature- and atmosphere dependent. Thus, this work focuses on a quantitative analysis of the temperature- and gas atmosphere-dependent phase transformation of tetragonal t-ZrO_2 into monoclinic m-ZrO_2 during heating–cooling cycles from room temperature to 1273 K. Synchrotron-based in situ X-ray diffraction (XRD) studies in gas atmospheres of different reduction strengths, namely, 5 vol% H_2/Ar, He, CO_2, and air, revealed a stabilizing effect of inert and reductive environments, directly yielding different temperature onsets in the phase transformation during cooling (i.e., 435, 510, 710, and 793 K for 5 vol% H_2/Ar, He, CO_2, and air, respectively). Rietveld refinement shows a direct influence of the atmosphere on grain size, unit cell, and weight fraction of both polymorphs in the product composite matrix. The tetragonal-to-monoclinic (t–m) phase transformation is suppressed in the sample heated only up to ~850 K, independent of the gas atmosphere. The results of ex situ XRD, transmission electron microscopic, electron paramagnetic resonance, and oxygen titration experiments confirmed that the phase transformation is accompanied by a change in the crystallite/particle size and the amount of lattice defects (i.e., oxygen vacancy). Due to the different onset temperatures, a complex interplay between kinetic limitations of phase transformation and grain sintering yields different pathways of the phase transformation and, eventually, very different final crystallite sizes of both t-ZrO_2 and m-ZrO_2.

KEYWORDS
defect chemistry, dissolved hydrogen, oxide non-stoichiometry, temperature-programmed reduction and oxidation, X-ray diffraction

1 | INTRODUCTION

ZrO_2 is one of the most extensively studied oxides with diverse applications ranging from structural ceramics to bioceramics, sensors, and catalysis.[1–9] For all of them, a deep understanding of structural stability under various environments is one of the pre-requirements, the structural transformation depends, in turn, on the surface and bulk chemistry of ZrO_2 polymorphs. Under ambient pressure conditions, three ZrO_2 polymorphs are known: a monoclinic polymorph (m-ZrO_2, space group $P2_1/c$, No. 14), which is thermodynamically stable at ambient temperature, and high-temperature tetragonal (t-ZrO_2, $P4_2/nmc$, No. 137) and cubic (c-ZrO_2, $Fm\bar{3}m$, No. 225) polymorphs. The latter two are metastable and are usually stabilized by dopants such as Y^{3+} and Ce^{4+} cations. Two other mechanisms widely discussed in the literature are focused on the influence of the defect chemistry (especially oxygen vacancies) and crystal size. Despite both being a matter of controversial discussions, there is a common understanding that there is a critical concentration of oxygen vacancies and a critical size limit for the stabilization of both metastable polymorphs. A canonical example is the critical size threshold of about 33 nm for t-ZrO_2.[3] Both thermodynamic models and DFT calculations stress out the dependence of critical size on the crystal shape of initial and final phases as well as the surrounding environment.[10,11]

The tetragonal-to-monoclinic (i.e., t-ZrO_2 → m-ZrO_2) phase transformation is widely exploited for ceramic toughening[12] and heterogeneous catalysis.[13–15] For instance, the t-ZrO_2 → m-ZrO_2 phase transformation in Pd/ZrO_2 and Au/ZrO_2 catalysts is accompanied by an increase in the concentration of surface oxygen vacancies that in turn enhances the catalytic activity in the CO and methane oxidation.[13,14]

As the understanding of the polymorphism on the microscopic level is a prerequisite for the rationalized design of applications, a great deal of work in the last decades has been devoted to unraveling the mechanistic details of the t-ZrO_2 → m-ZrO_2 phase transformation.[8,9,16–26] It has been classified as a so-called martensitic, that is, athermic diffusionless phase transformation, where sheer forces alter the structure without changes in the concentration of dissolved components.[27] Besides, a few in situ X-ray diffraction (XRD) studies on the phase stability of pure t-ZrO_2 at high temperatures are limited to air.[28–30] Further in situ XRD experiments under different gas atmospheres are therefore required to understand the structural stability and phase transformation of t-ZrO_2 under gas atmospheres relevant to the catalytic and solid oxide fuel cell (SOFC) applications (e.g., H_2, CO_2, and O_2). Thus, in a recent work, the gas-phase dependence of this phase transformation under oxidative, reductive, or inert gas atmospheres has been addressed on a mere qualitative basis.[31] Special focus was put on the comparative behavior in different oxidative and reductive environments to elucidate the kinetic stability of tetragonal ZrO_2 and also in catalytically and technologically relevant gas atmospheres. Due to the stabilization of structural defects, especially inert atmospheres suppress the transformation into m-ZrO_2 during cooling of the preheated t-ZrO_2 phase, even at temperatures as high as 1273 K.[31] Oxidative atmospheres favor the transformation t-ZrO_2 → m-ZrO_2, and in reductive atmospheres (such as CO or H_2), the m-ZrO_2 fraction increases after a heating-cooling cycle, which was explained by the formation of (oxy-)carbides or dissolved hydrogen species that can be considered as a unique form of defect alteration and blockage.[31] However, the structural consequences on a (semi)quantitative level have not been addressed in detail yet. This especially encompasses the crystal size and lattice parameter alterations. A possible quantitative analysis between oxygen vacancy concentration and the associated structural stability in relevant gas atmospheres has not been attempted so far, which is crucial in clarifying the role of structural defects in stabilizing t-ZrO_2.

To close this knowledge gap, we present here a concise comparative aberration-corrected electron microscopy and in situ XRD study, which is directly correlated with oxygen titration measurements and electron paramagnetic resonance (EPR) to elucidate the influence of structural defects on phase transformations in ZrO_2. Both the electron microscopy and XRD experiments are designed in a very sophisticated way to extract the necessary information. As for the former, a delicate Fourier-transform analysis of high-resolution (HR) electron microscopy images was necessary to discriminate between t-ZrO_2 and m-ZrO_2 in the morphological and structural composite mixture after the respective annealing treatments. To elucidate the necessary structural information during sintering/annealing (i.e., lattice parameters, crystallite size, and phase composition), dedicated synchrotron-based experiments were carried out.

2 | EXPERIMENTAL PROCEDURES

2.1 | Materials

The zirconia precursor was synthesized by a sol–gel method from zirconium(IV) isopropoxide (isopropanol adduct, 99.9% Zr, and strem chemicals) dissolved in isopropanol (Finne Gatt-Koller, 99.98%) and quenched with

water, as described previously.[30] The resulting gel was then dried to obtain the amorphous zirconia precursor that was calcined at 723 K in air to produce phase-pure t-ZrO_2. The latter was subsequently heated in a tube furnace with a Schlenk tube under flowing 5 vol% H_2/Ar, He, CO_2, and air (approximately 40 mL/min) at two different temperatures of 850 and 1200 K, holding for 10 min before cooling to room temperature. A heating/cooling rate of 100 K/h was used for all treatments.

2.2 | Electron microscopy

The structure of the ZrO_2 nanoparticles was investigated by high-resolution transmission electron microscopy (HRTEM) carried out on an aberration-corrected FEI Titan3 80-300 microscope operated at 300 keV electron energy. The identification of the ZrO_2 particles and the phase assignment is entirely based on the two-dimensional Fourier transformation (FT) analysis of HRTEM images recorded from particle agglomerations on the sample followed by the correlation with the calculated diffraction pattern of oriented bulk t-ZrO_2 and m-ZrO_2 polymorphs. The inverse FT was applied to identify the size and location of the respective ZrO_2 polymorph domains within the composite matrix. The analysis has been repeated for all treatments and results in particle size histograms consisting of between 200 and 700 individual particles. Despite most ZrO_2 nanoparticles exhibiting a tetragonal structure characterized by larger diameters as compared with m-ZrO_2 nanoparticles, the distinction between the two ZrO_2 polymorphs cannot be performed directly within HRTEM images of highly agglomerated particle ensembles. The structure analysis of an ensemble containing a mixture of particles with t-ZrO_2 and m-ZrO_2 structures is based on the following considerations: HRTEM images of such nanoparticle ensemble are recorded, and Fourier transformed. A given $(h\,k\,l)$ Bragg reflection, which can be unambiguously assigned either to the t-ZrO_2 or to the m-ZrO_2 polymorph in the FT image, is then selected, and its intensity is artificially enhanced. The inverse Fourier transform image (called Fourier-filtered (FF) image) is calculated by taking only this $(h\,k\,l)$-reflection into account. The FF image reveals both the size and the location of the corresponding t-ZrO_2 or m-ZrO_2 domain within the ensemble. Lastly, the FT–FF particle identification is verified by determining the structure of that individual particle inside the corresponding location on the initial HRTEM image of the ensemble by comparing its FT with the calculated diffraction pattern of either the t-ZrO_2 or the m-ZrO_2 phases.

The irradiation with the high-energy electron beam can induce the particle sintering within agglomerated aggregates and, influence by that, the size of single crystalline domains with t-ZrO_2 or m-ZrO_2 structure determined by TEM experiments. The sintering mechanisms that have to be considered here are the coalescence and the oriented attachment of single particles. The sintering by coalescence, where there is no particular relation in the lattice plane orientation at boundaries of single crystalline domains that grows, is not expected to modify the size of single crystalline domains with either the t-ZrO_2 or the m-ZrO_2 structure as determined by TEM experiments. On the contrary, the orientated attachment (OA) of particles, where a common crystallographic alignment of the lattice plane orientation at boundaries of single crystalline domains that grows allows for continuous crystallographic planes within the larger domain, will result in an increase of the particle size determined by TEM.

To avoid the OA sintering of particles due to the irradiation with the high-energy electron beam during the acquisition of HRTEM images, different regions of one and the same sample were analyzed, which were not illuminated during previous measurements. All microscope alignments are carried out on a sample region, which is not considered for the data evaluation. The sample is then moved to an adjacent region that was not previously exposed. The image is immediately taken without refocusing. By using this procedure, the total illumination time (choice of region and recording the image) becomes shorter than 2 s, avoiding the OA sintering of particles in agglomerates.

2.3 | In situ X-ray diffraction

The in-situ high-temperature synchrotron XRD experiments in CO_2, He, air, and 5 vol% H_2 in argon flow were performed at beamline 12.2.2 at the Advanced Light Source and Lawrence Berkeley National Labs. The in-situ diffraction patterns were collected in the angle-dispersive transmission mode with a focused 25 keV monochromatic beam (λ = 0.4959 Å/50 μm spot size). The sample powder was heated in 700 μm quartz capillaries under a continuous gas flow injected through another 300 μm capillary with a cut-open end. The capillary is heated in an infrared-heated SiC tube furnace described elsewhere.[32,33] Diffraction patterns are recorded by a Perkin Elmer flat panel detector (XRD 1621, dark image and strain correction) every 25 s during the heating and cooling cycle. The amorphous zirconia precursor was in situ heated first to 723 K inside the capillary under air flow until crystallization to t-ZrO_2 was completed. The obtained phase-pure t-ZrO_2 was then reheated in the target gas (i.e., CO_2, He, and 5 vol% H_2 in Ar). The reference t-ZrO_2

specimen synthesized using the procedure described in 2.1 was used for the in situ XRD experiment in the air.

2.4 | Electron paramagnetic resonance (EPR) measurements

Continuous wave (cw) EPR measurements at X-band (9.78 GHz) and Q-band (34 GHz) frequencies were conducted at room temperature in quartz tubes of 2.9 mm outer diameter, with a Bruker B-ER420 spectrometer upgraded with a Bruker ECS 041XG or Bruker ER051 QG microwave bridge and a lock-in amplifier (Bruker ER023M), a modulation amplitude of 1 G and a modulation frequency of 100 kHz were applied with a Bruker TE_{102} or an ER051QT resonator. All EPR spectra were normalized to the sample mass.

2.5 | Thermogravimetry (TG) and mass spectrometry (MS) measurements

Thermogravimetry analysis coupled with a mass spectrometry (TGA-MS) measurements were conducted in STA 409 PC LUXX (Netzsch) and a PFEIFFER OMNISTAR GSD320 O1 (Pfeiffer Vacuum GmbH), equipped with an iridium filament and heated lines. The samples were heated up to 1200 K in air and 5 vol% H_2/Ar atmospheres using a heating rate of 5 K/min.

2.6 | Temperature-programmed oxygen titration

The titration of oxygen vacancies produced in t-ZrO_2 by various reduction treatments was performed by O_2-temperature-programmed oxidation (O_2-TPO). For this experiment, the reduced sample was exposed to a defined amount of O_2 that had been pre-dried in a 163 K cooling trap. The sample was then submitted to a temperature program consisting of three phases. In the first phase, the sample was heated from room temperature to approximately 1220 K at a rate of 5 K min^{-1}. The maximum temperature was maintained for 10 min before the sample was allowed to cool back down to room temperature at a rate of 5 K min^{-1}. As the setup did not allow for active cooling, the cooling rate decreased steadily at temperatures below 373 K. The O_2 uptake at each given point during the experiment was determined by the pressure drop in the system—based on the ideal gas equation—which required an He calibration experiment under O_2-TPO conditions in order to determine the sample temperature-dependent effective volume of the reactor.

3 | RESULTS AND DISCUSSION

3.1 | Structural evolution of t-ZrO_2 in different atmospheres from in situ XRD

To follow the structural evolution of t-ZrO_2 (and, thus, its phase stability and propensity to phase transformation) and to directly assess the influence of structural defects on such transformations, the t-ZrO_2 samples were subjected to the same heating-cooling cycle in gas atmospheres (i.e., 5 vol% H_2/Ar, He, CO_2, and air) relevant to catalysis and SOFC applications. The corresponding in situ XRD patterns collected during cooling from 1273 K are displayed in Figure 1. The Rietveld refinement of the in situ XRD data allows for extracting detailed information about the domain size, unit cell volumes, and amount of t-ZrO_2 and m-ZrO_2 polymorphs, as shown in Figure 2.

As can be seen in Figure 1, the t-ZrO_2 is stable upon heating to 1273 K in all atmospheres and partially transforms to m-ZrO_2 only upon cooling. In all cases, the final samples—obtained upon cooling to room temperature—consist of a mixture of t-ZrO_2 and m-ZrO_2 with different weight fractions depending on the gas environment.

As shown in Figure 2A, the transformed t-ZrO_2 fraction (i.e., m-ZrO_2) was found to be approximately 18, 56, 93, and 93 wt.% after heating in 5 vol% H_2/Ar, He, CO_2, and air, respectively. A similar trend is observed for the onset of phase transition temperatures (when the phase transition t → m-ZrO_2 starts at the earliest): Here, this temperature is highest at 793 K in air, followed by 710, 517, and 435 K for heating in CO_2, He and 5 vol% H_2/Ar, respectively. These results indicate that oxidative gases, such as air and CO_2, facilitate the t → m-ZrO_2 transformation, whereas the inert (i.e., He) and reducing (i.e., 5 vol% H_2/Ar) gas atmospheres stabilize t-ZrO_2 in the final mixtures as well lower the onset temperature of t-ZrO_2 → m-ZrO_2 phase transition during the cooling process. The reasons could be two-fold: (i) the stabilization of oxygen vacancies and carbon doping in reductive environments and (ii) the influence of different atmospheres on the crystallite size of t-ZrO_2.

As displayed in Figure 2B, the evolution of the tetragonal unit cell volume reveals additional interesting features. Upon heating in all gas mixtures under study, a distinct "plateau" between 600 and 900 K appears. This feature is well known for other oxides, such as CeO_2, $La_{0.6}Sr_{0.4}FeO_3$, and La_2NiO_4,[34–36] where the removal of oxygen from the lattice in reducing atmospheres results in a decreased unit cell volume. The sharp increase in the unit cell volume above 900 K may be due to the reduction of Zr^{4+}–Zr^{3+} (which is accompanied by an increase in the ionic radius of the cations) to compensate for the thermal oxygen loss

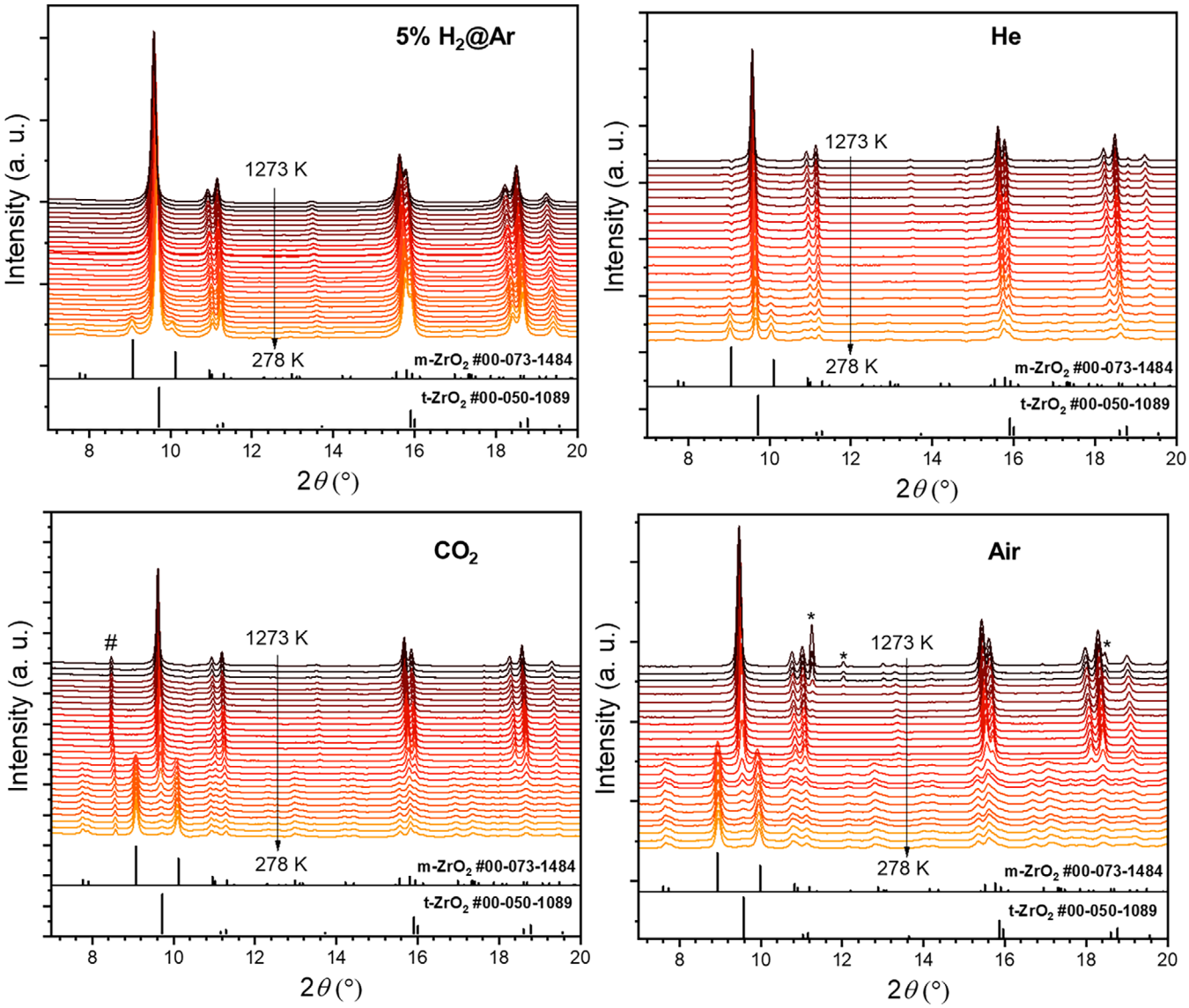

FIGURE 1 In situ X-ray diffraction (XRD) patterns of t-ZrO_2 samples during cooling from 1273 to 278 K display phase transformation t-ZrO_2 → m-ZrO_2 under flowing of 5 vol% H_2/Ar, He, CO_2, and air atmospheres. Calculated diffraction patterns for t-ZrO_2 (PDF 00-050-1089) and m-ZrO_2 (PDF 00-073-1484) are shown at the bottom of each plot, whereas the symbols (*) and (#) refer to the peaks of quartz SiO_2 and SiC, respectively (both used as sample holders in the in situ XRD experiments).

between 600 and 900 K. Although air and CO_2 are oxidizing atmospheres, the loss of oxygen and reduction of Zr^{4+} into Zr^{3+} can occur by the oxidation of carbon residue originating from the zirconia precursor. This reduction by carbon-containing impurities in an oxidizing atmosphere, such as air and CO_2, has previously been reported for several transition metal oxides.[34,37,38] It is worth noting that the zirconia precursor was calcined at 723 K prior to the in situ XRD experiments, this temperature was insufficient for the full oxidation of all carbon residues in the specimens. During cooling, a linear contraction of the unit cells is observed in all atmospheres. However, as shown in Figure 2B for all atmospheres, the untransformed t-ZrO_2 shows a larger unit cell volume during cooling than that determined during the heating step for the initial t-ZrO_2 phase at the same temperature. Moreover, as shown in Figure S1, the XRD reflections corresponding to t-ZrO_2 observed in the pattern collected at 850 K during cooling are shifted to higher interplanar distances if compared with those observed at the same temperature during heating. These results confirm that the initial structure of t-ZrO_2 is altered during heating due to the oxygen/carbon loss and the partial reduction of Zr^{4+} into Zr^{3+}. At lower temperatures, the calculation of the unit cell volume of t-ZrO_2 in air and CO_2 atmospheres is accompanied by large standard deviations due to the significant decrease of the weight fraction of the t-ZrO_2 so that its XRD reflections are becoming more and more superimposed by the large

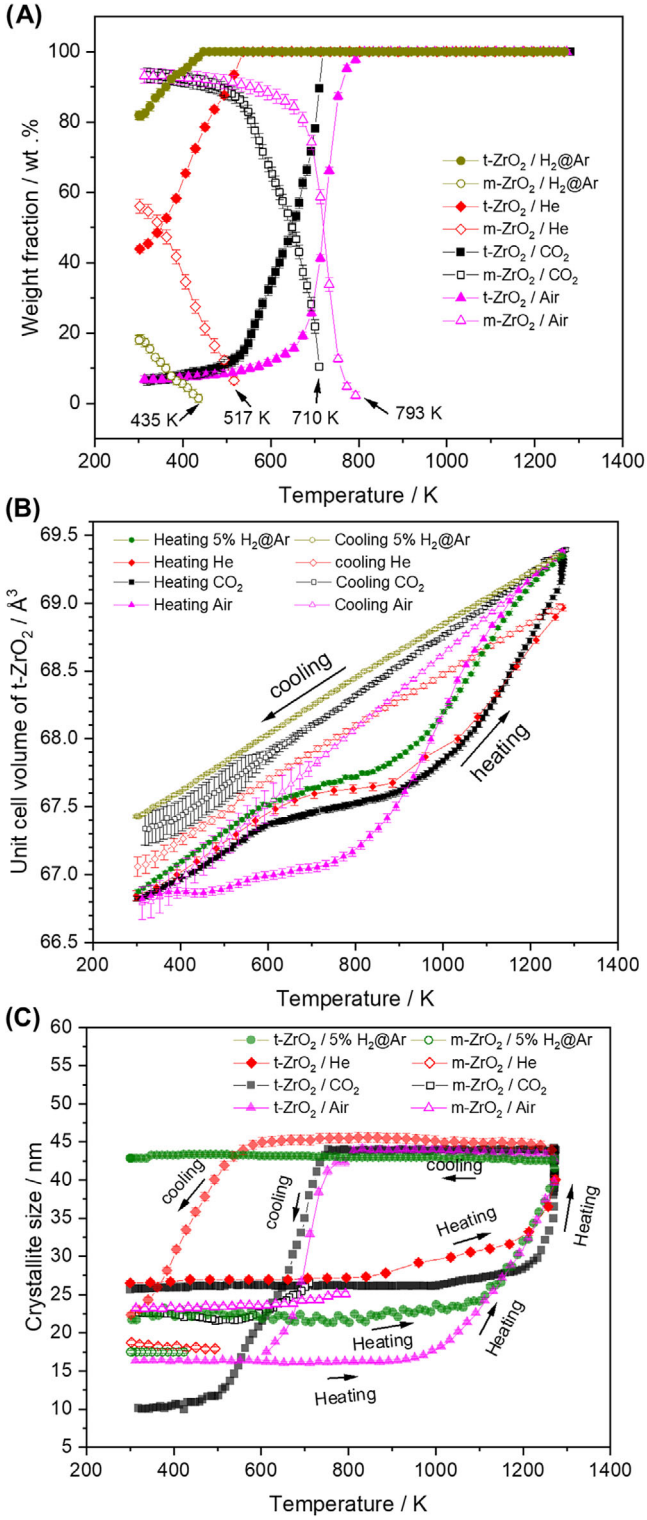

FIGURE 2 Results of the Rietveld refinement of the X-ray diffraction (XRD) data from Figure 1: (A) weight fraction, (B) unit cell volume, and (C) crystallite size of t-ZrO_2 and m-ZrO_2 polymorphs.

number of reflections of m-ZrO_2, rendering Rietveld refinement difficult, thus increasing the error bars.

Figure 2C reveals that the evolution of crystallite (domain) size during heating is similar for all gaseous environments examined in this work, the difference appears only upon cooling. The crystallite size of the initial t-ZrO_2 samples is calculated to be in the range between 16.5 and 25.5 nm, which is smaller than the critical size (~30 nm) required to stabilize the t-ZrO_2 phase, as suggested previously.[3] The crystallite size remains almost unchanged during heating up to 1000 K in all atmospheres before significantly increasing to ~44 ± 1 nm at 1273 K in all atmospheres. During cooling, the crystallite size remains constant before decreasing again, coinciding with the transformation of t-ZrO_2 into m-ZrO_2. Despite similar maximum crystallite sizes of t-ZrO_2 being determined in all atmospheres, a lower transformation temperature and weight fraction of m-ZrO_2 were observed for 5 vol% H_2/Ar and He, as compared to CO_2 and air. These results suggest that the interaction of different gas atmospheres with point defects in t-ZrO_2 could also be another reason for the destabilization of this polymorph.

3.2 | Evolution of crystallite sizes of t-ZrO_2 and m-ZrO_2 from aberration-corrected electron microscopy

To study the influence of crystallite size and lattice defects on the phase transformation of t-ZrO_2, the material was heated at two temperatures, that is, 850 and 1200 K, in different atmospheres. As shown in Figure S2, the obtained samples after heat treatment possess visibly different colors, which may be attributed to their different crystallite size, phase composition, and deviation from the stoichiometric composition. Agreeing with in situ XRD results, the t-ZrO_2 phase was found to be stable in all samples heated at 850 K regardless of the used atmospheres (Figure S3). No remarkable change in the crystallite size was observed either, as revealed by Rietveld refinement analysis (Table 1). In contrast, the t-ZrO_2 phase is partially transformed into the m-ZrO_2 phase, when the samples are treated at 1200 K (Figure S3). The weight fraction and crystallite size of untransformed t-ZrO_2 and formed m-ZrO_2 phases are found to be influenced by the different atmospheres (Table 1). These results agree with the results of in situ XRD experiments (Figure 2).

The determination of the crystallite sizes of t-ZrO_2 and m-ZrO_2 polymorphs in the TEM experiments is severely hampered by the particle agglomeration and the structural defectiveness of the ZrO_2 material. Therefore, especially for those samples/treatments, where a composite of both polymorphs is expected, an analysis method that

TABLE 1 Domain size and weight fraction of t-ZrO_2 and m-ZrO_2 polymorphs in ZrO_2 specimens treated at 850 and 1200 K in different atmospheres as obtained by HRTEM and X-ray diffraction (XRD) analysis.

		m-ZrO_2			t-ZrO_2		
		Domain size (nm)		Weight fraction	Domain size (nm)		Weight fraction
Temp (K)	Atmosphere	TEM	XRD/RR	(%)	TEM	XRD/RR	(%)
723	Air		–	–	5.2 ± 1.6	12.0 ± 1.2	100
850	5 vol% H_2/Ar		–	–	7 ± 3	22.4 ± 2.2	100
	CO_2		–	–	8 ± 3	22.4 ± 2.1	100
	Air		–	–	5.2 ± 1.6	12.0 ± 1.2	100
1200	5 vol% H_2_Ar	6 ± 2	8.3 ± 1.8	11.3 ± 1.2	18 ± 4	30.6 ± 2.2	88.7 ± 1.6
	He	7 ± 3	13.3 ± 1.7	12.0 ± 1.1	17 ± 4	30.2 ± 2.2	88.0 ± 1.7
	CO_2	23 ± 5	18.6 ± 1.6	78.5 ± 1.2	7 ± 2	14.1 ± 1.5	21.5 ± 1.9
	Air	14 ± 4	21.6 ± 1.6	91.4 ± 1.7	6 ± 2	7.5 ± 1.5	8.6 ± 1.2

Abbreviation: TEM, transmission electron microscopy.

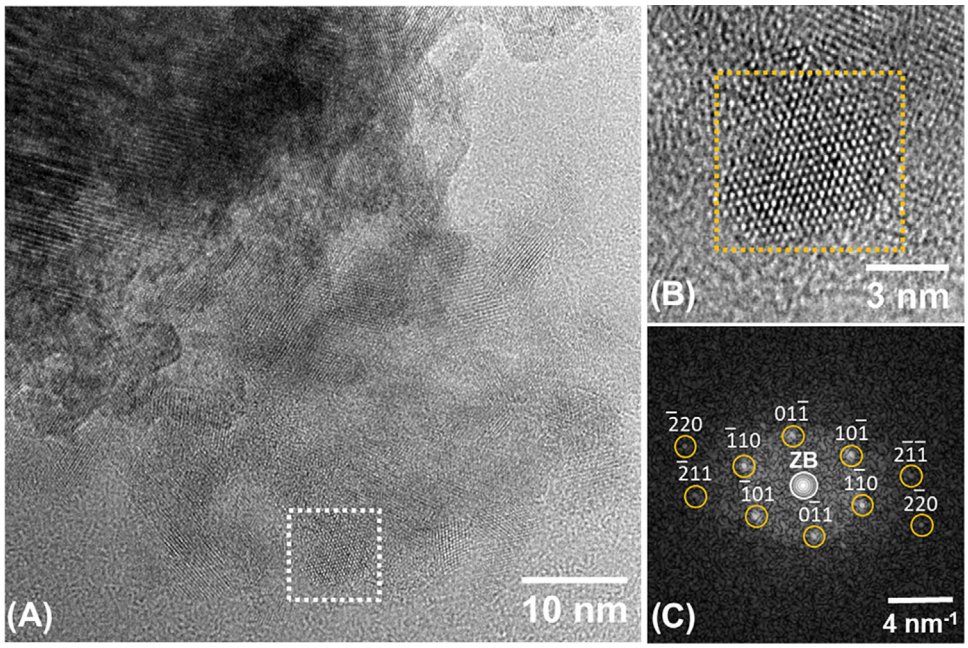

FIGURE 3 (A) Transmission electron microscopy (TEM) overview image of a particle agglomeration on the untreated phase-pure t-ZrO_2 sample. Panel B: magnified HRTEM image of the crystalline t-ZrO_2 domain marked with the white frame in (A), Panel C: the Fourier transformation (FT) pattern of the particle marked by the orange frame in (B) and calculated diffraction pattern with Miller indices for the t-ZrO_2 phase in the [111]-zone axis (orange circles). The white circle indicates the zero-order beam (ZB).

reproducibly allows distinguishing between microcrystals of both modifications needed to be used. The method of choice, which has been outlined in detail in the experimental section, is based on FT–FF analysis of HRTEM images and is exemplified in the following. For materials where only one crystalline structure/one polymorph is expected, such as the untreated t-ZrO_2 reference material, this sequence of analysis is easier. To illustrate the procedure applied to determine the particle size in this case, a demagnified TEM overview image of such a particle agglomerate with rounded individual grains apparently "glued" together was considered in Figure 3 (Panel A). To identify the size of individual particles with tetragonal ZrO_2 structure, a representative region marked with the white frame in Figure 3A is shown magnified on the HRTEM image in Figure 3 (Panel B). Subsequently, the FT of the particle (orange frame) in Figure 3B has been calculated and shown in Figure 3 (Panel C). According to this analysis, the whole nanoparticle is a single ZrO_2 monocrystal with a tetragonal structure, as indicated by the good agreement between its two-dimensional Fourier transform and the calculated diffraction pattern of the bulk

tetragonal ZrO_2 (space group No. 137, $P4_2/nmc$, with lattice parameters of $a = b = 3.593$ Å and $c = 5.184$ Å) in the [1 1 1]-zone axis. Then, a diameter of 6.4 nm was determined for the single t-ZrO_2 monocrystal shown in Figure 3B. Similarly, the FT analysis of 453 monocrystals located on many HRTEM images recorded on the untreated t-ZrO_2 reference sample yielded the particle size histogram shown in Figure S4, with an average crystallite diameter of $\bar{D} = 5.4 \pm 1.6$ nm.

The steps of phase identification for samples containing a mixture of particles with both the t-ZrO_2 and m-ZrO_2 structures are highlighted in Figure 4 for a t-ZrO_2 sample treated in 5 vol% H_2/Ar atmosphere at 1200 K. According to the XRD results (see Figure S3 and Table 1), a mixture of t-ZrO_2 and m-ZrO_2 polymorphs is prevalent in this sample after completing the heating-cooling cycle. The TEM analysis, therefore, must ensure the elucidation of the structure and sizes of the nanocrystals of both polymorphs. In the following, the procedure used to determine the size and the location of an m-ZrO_2 domain is first described. As outlined in the experimental section, the first step is the recording of the HRTEM image of the prospective nanoparticle agglomeration (Figure 4A), followed by the calculation of its FT pattern (Figure 4B). The intensity of the $(1\ \bar{1}\ 0)$ reflection of m-ZrO_2 (which allows for unambiguous identification of the m-ZrO_2 phase) is artificially increased and used to calculate the $(1\ \bar{1}\ 0)$-FF image (Figure 4C). The comparison of the FF image (Figure 4C) with the initial HRTEM image (Figure 4D) directly allows for the identification of the crystal domains with the m-ZrO_2 structure. However, the FT–FF method is then verified by the structure determination of the whole domain selected using the FT–FF method (frame on Figure 4D), which must be single crystalline monoclinic ZrO_2. For that, the FT of the domain within the frame on the HRTEM image in Figure 4D is calculated (Figure 4E). The FT agrees with the calculated diffraction pattern of the bulk m-ZrO_2 (space group $P2_1/c$, No. 14, lattice parameters of $a = 5.145$ Å, $b = 5.208$ Å, $c = 5.311$ Å, and $\beta = 99.23°$) in the [1 1 6]-zone axis (Figure 4E). The size distribution of m-ZrO_2 domains within the t-ZrO_2 sample treated in 5 vol% H_2/Ar atmosphere at 1200 K determined using 316 particles located on many HRTEM images (Figure S5) results in an average diameter of about 6 ± 2 nm.

Similar analysis was further applied to determine the size of t-ZrO_2 domains in that sample. For simplicity reasons, only the verification step of the FT–FF method applied in the case of a t-ZrO_2 domain within a particle agglomerate on the t-ZrO_2 sample treated in 5 vol% H_2/Ar atmosphere at 1200 K (Figure 5A) is detailed in Figure 5. Accordingly, the whole nanoparticle domain of about 18 nm inside the frame in Figure 5B possesses the t-ZrO_2 structure, as indicated by the good agreement between its two-dimensional Fourier transform and the calculated diffraction pattern of the bulk t-ZrO_2 in the [3 1 1]-zone axis. The diameter distribution of t-ZrO_2 domains on this sample, determined by using 190 different particles, yields an average size of about 18 ± 4 nm.

Table 1 summarizes the results of the outlined analysis performed on samples treated in inert He, CO_2, air, and 5 vol% H_2/Ar atmospheres at 850 and 1200 K. Starting with an average domain size of 5.2 nm in the initial t-ZrO_2 material, it is directly revealed that treatments in any atmosphere up to 850 K do not cause a phase transformation to m-ZrO_2 and the average t-ZrO_2 domain size remains unchanged within the standard deviation, which agrees with results of Rietveld refinement analysis. However, the domain size determined from HRTEM analysis is slightly lower than that determined from XRD analysis. To explain that, it can be assumed that heating-cooling cycles of samples, which induce the OA sintering of particles within agglomerates, yield many grains with larger diameters but only an almost perfect single crystalline t-ZrO_2 or m-ZrO_2 structure. However, even a small misorientation of $(h\,k\,l)$ lattice planes in such a large OA grain may give rise to enough well-separated $(h\,k\,l)$ diffraction peaks of each small single crystalline domain in the FT pattern calculated by using the HRTEM image of the whole large grain. In this case, the size of single crystalline domains determined by TEM remains the same as that of the initial small domain sizes despite the fact that the OA sintering yields single grains with larger sizes. On the other side, the structure analysis of the XRD pattern measured from this sample will result in a larger size of coherent diffracting domains (larger crystallite size), when the misorientation of $(h\,k\,l)$ planes is similar to the variation of the $(h\,k\,l)$ lattice plane distances over the whole sample. In this case, whole large grains grown by OA will be interpreted as single crystalline domains. Thus, larger size values of single crystalline domains are determined by XRD as compared with the corresponding values determined by HRTEM.

3.3 | Influence of oxygen vacancies on the phase transformation

As the phase transformation of t-ZrO_2 might be linked to the oxygen vacancies and other point defects and EPR may allow for their detection, if the defects are paramagnetic, the EPR spectra of the samples treated at 850 and 1200 K in different atmospheres were measured. In the room temperature cw EPR measurements at 9.78 GHz (Figure 6A), a relatively narrow signal at around $g = 2.003$–2.004 was detected. This EPR signal previously reported for ZrO_2 materials has been attributed to electron trapping at an oxygen vacancy.[39–41] In agreement with this

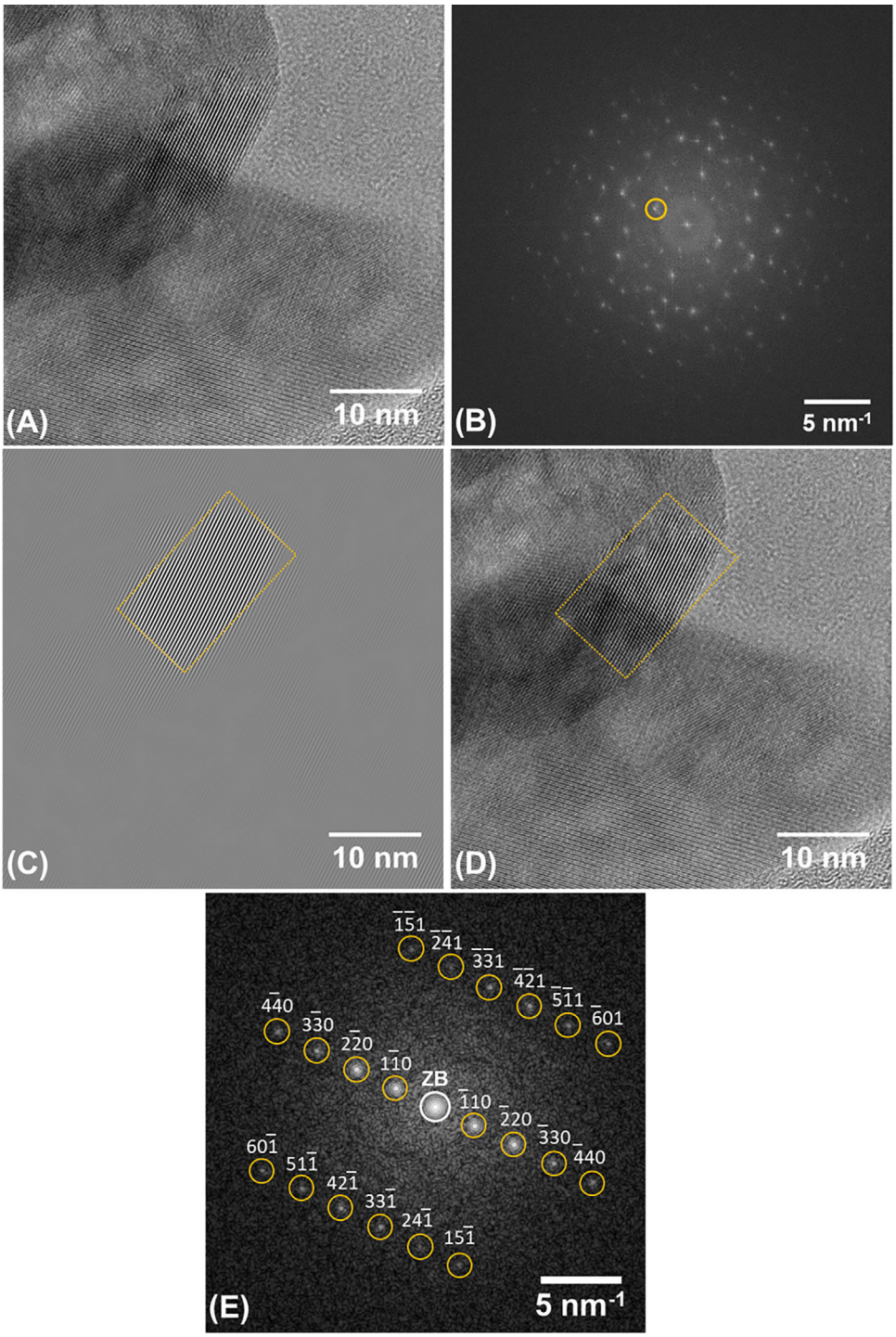

FIGURE 4 General sequence of the structure analysis procedure used to isolate the t-ZrO_2 or m-ZrO_2 nanocrystals and subsequently determine their individual sizes. As a representative example, a ZrO_2 particle ensemble on the sample obtained after treatment in 5 vol% H_2/Ar atmosphere at 1200 K is selected. Panel A: HRTEM image of the representative ZrO_2 nanoparticle agglomerate. Panel B: Corresponding Fourier transformation (FT) of the whole HRTEM image shown in Panel A with an orange circle indicating the $(\mathbf{1}\ \bar{\mathbf{1}}\ \mathbf{0})$ reflection of m-ZrO_2 phase. Panel C: Corresponding $(\mathbf{1}\ \bar{\mathbf{1}}\ \mathbf{0})$-Fourier-filtered (FF) image calculated by inverse FT of the FT pattern in C after an artificial increase in the intensity of the $(\mathbf{1}\ \bar{\mathbf{1}}\ \mathbf{0})$ reflection. Panel D: The HRTEM image shown in A with the frame marked and identified region of the m-ZrO_2 phase. Panel E: the FT pattern of the region marked by the orange frame in (D) and calculated diffraction pattern with Miller indices for the m-ZrO_2 phase in the [116]-zone axis (orange circles). The white circle indicates the zero-order beam (ZB).

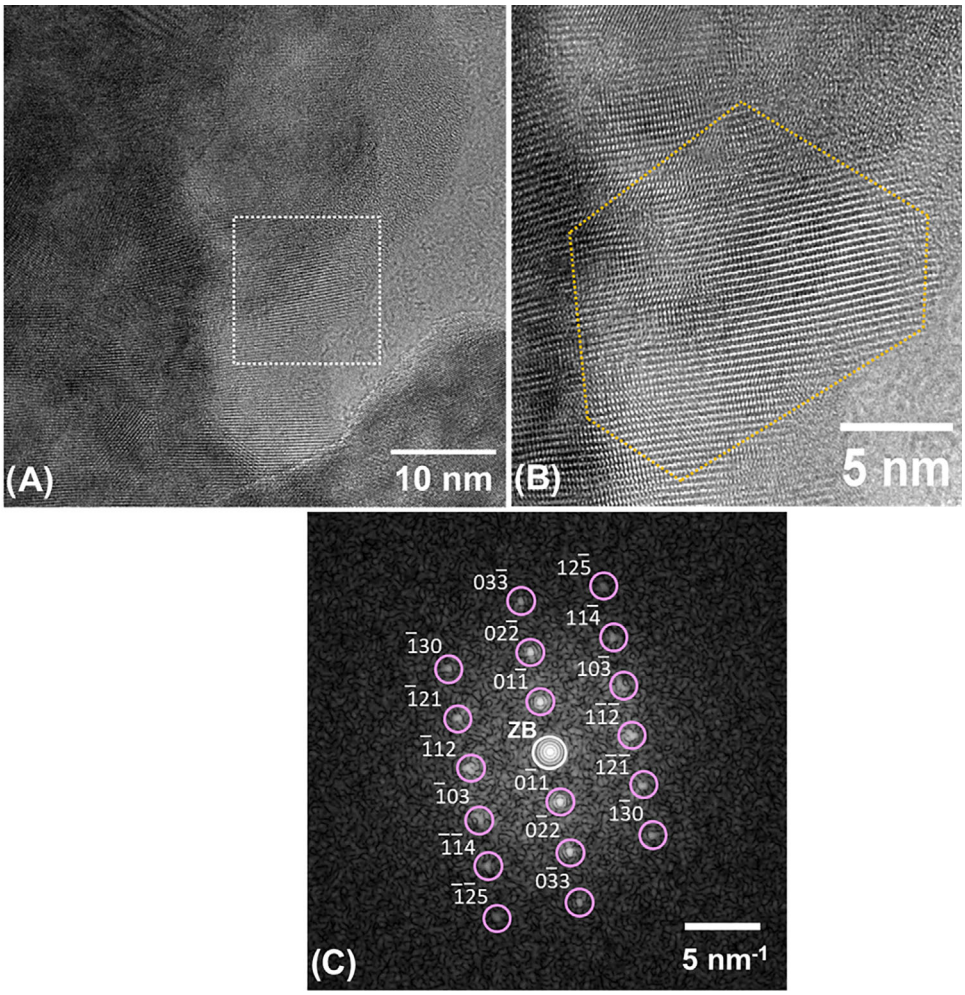

FIGURE 5 Panel A: HRTEM overview image of an aggregate within the sample containing a composite mixture of t-ZrO_2/m-ZrO_2 phases after a heating/cooling cycle up 1200 K in 5 vol% H_2/Ar atmosphere. Panel B: magnified HRTEM image of the region inside the frame in (A). The polygon gives a guide to the eye of a single t-ZrO_2 particle outline. Panel C: FT pattern of the polygonal region shown in Panel B and calculated diffraction pattern with Miller indices for the t-ZrO_2 phase in the [311]-zone axis (rosa circles). The white circle indicates the zero-order beam (ZB).

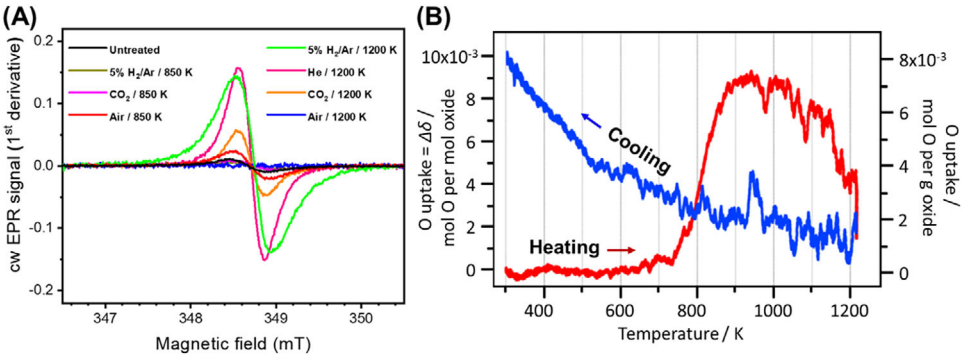

FIGURE 6 (A) Continuous wave (cw) electron paramagnetic resonance (EPR) measurements at room temperature of untreated t-ZrO_2 sample as well as the obtained samples after heating at 850 and 1200 K in different atmospheres (9.78 GHz mw frequency, modulation amplitude 1 G, and modulation frequency 100 kHz). (B) Results of the temperature-programmed oxygen titration experiments: Oxygen uptake by the specimen obtained by treating t-ZrO_2 in 5 vol% H_2/Ar at 1220 K is shown as mol O per mol oxide (representing the number of oxygen vacancies as deviation from the initial stoichiometry) and in mol O per g oxide.

assignment to paramagnetic oxygen vacancies, the sample heated to 1200 K in air does not show this signal, whereas the samples heated to 1200 K in 5 vol% H_2/Ar, He, and CO_2, that is, in less oxidative atmospheres, exhibited notable signal intensities (corresponding to approx. 5×10^{17} spins/g for the sample heated to 1200 K in 5 vol% H_2/Ar). For the samples heated to 1200 K, the signal intensity increases for more reductive atmospheres, that is, air < CO_2 < He < 5 vol% H_2/Ar. Thus, the results for samples heated to 1200 K agree overall well with the assignment to paramagnetic oxygen vacancies: In reductive atmospheres, oxygen loss may be facilitated, resulting in the formation of such paramagnetic oxygen vacancies, whereas more oxidative conditions may either lower their formation or even remove (pre-)existing oxygen vacancies at high temperature. For heating to 850 K, the intensity was overall lower for 5 vol% H_2/Ar (factor of approx. 20) and CO_2 (factor of approx. 4), which is consistent with a smaller oxygen loss at the lower temperature and thus, a smaller amount of paramagnetic oxygen vacancies, as compared to heating to 1200 K. This is also qualitatively consistent with the changes observed for the unit cell volume that indicate the oxygen loss to proceed for temperatures above 850 K. For heating in air, the sample heated to 850 K shows a higher signal intensity than for heating to 1200 K, indicating the temperature of 850 K is too low for the removal of these oxygen defects.

However, the signal intensity is also higher than those of the sample heated to 850 K in less oxidative atmospheres, which is surprising. The question arises if more than one type of paramagnetic oxygen species contribute to the signal. To gain further information on the measured signal, 34 GHz cw EPR measurements were conducted. These showed an increase in the ΔB_{pp} linewidth for all samples, as compared to the measurements at 9.8 GHz (see also Figure S6). This result suggests that a range of (slightly) different defects with the type and distribution depending on the heating conditions contributes to the observed signal. However, it should be noted that none of the samples heated either to 850 or 1200 K displayed signals attributable to Zr^{3+}.[39] A possible reason for the unexpected signal intensities of the samples heated to 850 K could be connected to residual carbon impurities that react differently in the various atmospheres, that is, in air the reaction of residual carbon could induce the formation of paramagnetic defects, such as oxygen vacancies, at low temperatures that are removed in air at higher temperatures after the residual carbon is removed. The presence of residual carbon in the initial untreated ZrO_2 sample after calcination of the precursors at 723 K is indicated by its brownish color (Figure S2) and, moreover, by TG–MS analysis (Figure 7). The t-ZrO_2 specimen exhibits a small weight loss (~2.5 wt.%) during heating from room temperature to about 800 K in both 5 vol% H_2/Ar and air, which can be assigned to the desorption of physically absorbed water (m/z = 18) and gases such as CO_2 (m/z = 44). Although the release of absorbed water takes place until 400 K, the desorption of CO_2 continues up to ~800 K, agreeing with previous studies.[31,42] At higher temperatures, the weight loss, which reaches ~3.8 wt.% at 1200 K—is due to the loss of lattice oxygen and/or the removal of carbon residue in the samples as indicated from the released gaseous species, such as CO_2 (m/z = 44) in air and CO_2 and/or CH_3CHO (both m/z = 44) and $-CH_3$ (m/z = 15) fragments in 5 vol% H_2/Ar atmosphere. This result is in good agreement with the in situ XRD results (Figure 2B), which show a significant chemical expansion in the t-ZrO_2 lattice above 850 K due to the reduction of Zr^{4+}–Zr^{3+} to compensate for the loss in oxygen lattice. These results reveal that reheating this initial sample at 850 K in air resulted in the oxidization of these carbon species by combining "oxygen" from the gas phase and the lattice, thereby creating oxygen vacancies.

In contrast, the oxidation of carbon species is not favorable in reducing/inert (e.g., 5 vol% H_2/Ar, and He) and CO_2 (oxidation of C by CO_2 is thermodynamically favorable at temperatures >950 K[43]) atmospheres at this low temperature (850 K). As shown in Figure 7B, high amounts of carbon species are also released as gaseous hydrocarbon species (e.g., $-CH_3$), which is not observed for heating in air. Thus, the TG–MS analysis clearly reveals differences for the reaction of carbon species in the various atmospheres. In combination with EPR, these results suggest that the desorption of the gaseous hydrocarbon species is not connected with a formation of (EPR-active) oxygen vacancies. At higher temperatures (e.g., 1200 K), the removal of lattice oxygen by carbon species and/or H_2 will be facilitated in reducing/inert atmospheres (e.g., 5 vol% H_2/Ar and He), whereas oxidizing atmospheres (e.g., air and CO_2) allow for replenishment of oxygen vacancies by oxygen atoms in the atmospheres. However, as generating oxygen atoms in the CO_2 atmosphere is less favorable than in air and the reducing effect of CO formed due to the reaction of CO_2 with C, a high amount of oxygen vacancies remains in the sample even after heating at 1200 K. The change in the color of the samples treated at 1200 K from black, to gray to white (Figure S2) by changing the atmosphere from 5 vol% H_2/Ar and He to CO_2 to air in accordance with the amount of oxygen vacancies in these samples,[44] consistent with the EPR results.

To elucidate the influence of oxygen non-stoichiometry on the stabilization of t-ZrO_2 polymorph, temperature-programmed oxygen titration experiments in various inert and reductive environments have been performed in an identical manner to the TEM and in situ treatments. As outlined in the experimental section, t-ZrO_2 was treated in

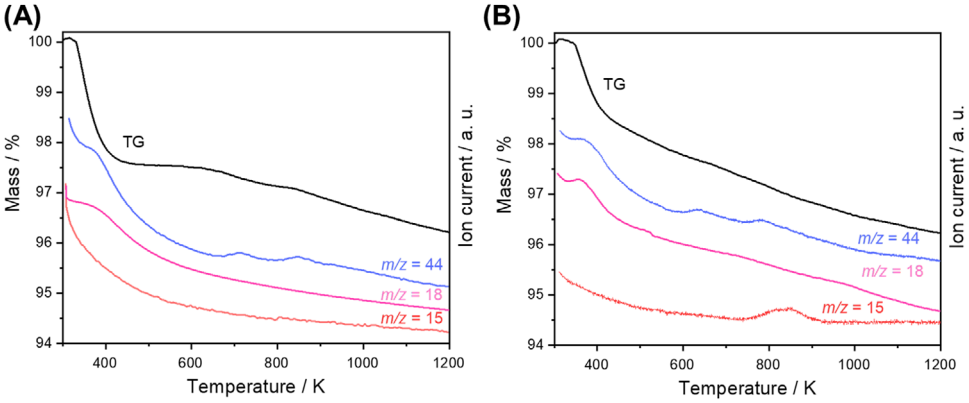

FIGURE 7 Thermogravimetry analysis (TGA) measurements coupled with mass spectrometry for t-ZrO_2 during heating in (A) air and (B) 5 vol% H_2/Ar.

either He or H_2/Ar to induce reduction and subsequently, oxygen was used to refill the oxygen vacancies formed and, hence, to calculate the oxygen non-stoichiometry resulting from the treatments. Figure 6 shows a representative example of such an experiment after treatment in 5 vol% H_2/Ar up to 1220 K (as the general outline of the experiments is similar, the representative results of only one are shown). During heating, oxygen replenishment sets in at around 600 K and is strongly accelerated up to 850 K, above that thermal removal of oxygen restarts up to the highest temperatures. Upon re-cooling to room temperature, reuptake of oxygen sets in and, depending on the treatments, results in a final value of between 0.0046 (H_2/Ar @ 850 K) and 0.0098 (H_2/Ar @ 1220 K) mol oxygen per mol oxide. These obtained final values are intrinsically explainable, as the higher the reduction temperature in hydrogen, the larger the non-stoichiometry, and a treatment in He at 1220 K reduces t-ZrO_2 slightly more than a treatment in H_2 at 850 K (0.0070 mol O per mol oxide is determined for He @1220 K). Hence, the obtained trend is $H_2/Ar_{1220\,K} > He_{1220\,K} > H_2/Ar_{850\,K}$, resulting in reduced samples with stoichiometries of $ZrO_{1.9902}$, $ZrO_{1.9930,}$ and $ZrO_{1.9954}$, respectively. This indicates that after any reductive treatment, the resulting ZrO_2 material remains de facto largely unreduced. Note that the term "ZrO_2" is used to denote the material as the oxygen titration experiments do not allow to discriminate between t-ZrO_2 and m-ZrO_2. As outlined in Table 1, the weight fraction of t-ZrO_2 after the treatment in either H_2 or He at 1200 K is similar (~89 wt.%) and remains at 100 wt.% after the treatment in H_2 at 850 K. It should be noted that only a small fraction of all oxygen vacancies (approx. 1% for the sample heated in 5 vol% H_2/Ar to 1200 K) contribute to the observed EPR signal, whereas the remainder is EPR-inactive. Correlating these findings with the TEM results indicates that although oxygen non-stoichiometry plays a crucial role in stabilizing t-ZrO_2, further introduction of such oxygen vacancies by reduction treatments is limited. Consequently, we infer that the propensity to phase transformation t-ZrO_2 → m-ZrO_2 is essentially governed by the stability of the existing defects (e.g., as a result of the preparation pathway) and less so by the introduction of further vacancies, for example, by reduction, *strongly entangled* with particle size evolution.

In this respect, we emphasize that no structural or morphological changes have been observed for t-ZrO_2 up to 850 K. After treatments in either air or CO_2 at 1200 K, m-ZrO_2 appears in the product mixture and exhibits a much larger particle size of around 17-18 nm compared to t-ZrO_2. Upon treatment in either inert (He) or reductive (H_2/Ar) atmospheres, the average particle/crystallite sizes are, in fact, reversed. The question now arises of how to interpret this rather peculiar phenomenon. For analysis, it is worthwhile to readdress three features that are already known for the gas-phase dependent phase transformation: (1) t-ZrO_2 is stabilized at small particle sizes (roughly d < 30 nm), (2) the phase transformation takes place upon cooling, and (3) t-ZrO_2 is stabilized by defects, in particular, by oxygen vacancies.

Based on the results discussed above, we suggest the transformation mechanism of t-ZrO_2 into m-ZrO_2 upon heating and cooling in different atmospheres as presented in Figure 8. Although the crystallite size of t-ZrO_2 phase increases to ~44 ± 1 nm upon heating to 1273 K, which is higher than the critical size (~30 nm) previously suggested to stabilize the t-ZrO_2 phase,[3] no phase transformation occurs. This can be due to a high amount of oxygen vacancies generated upon loss of lattice oxygen in the reducing atmospheres as well as upon removal of carbon species, the oxygen vacancies are distributed over the entire volume of the t-ZrO_2 crystallites. Upon cooling, the oxygen from the oxidizing atmospheres (e.g., air and CO_2) refills both surface and volume oxygen vacancies, transforming almost the entire t-ZrO_2 crystallites into m-ZrO_2 phase. In

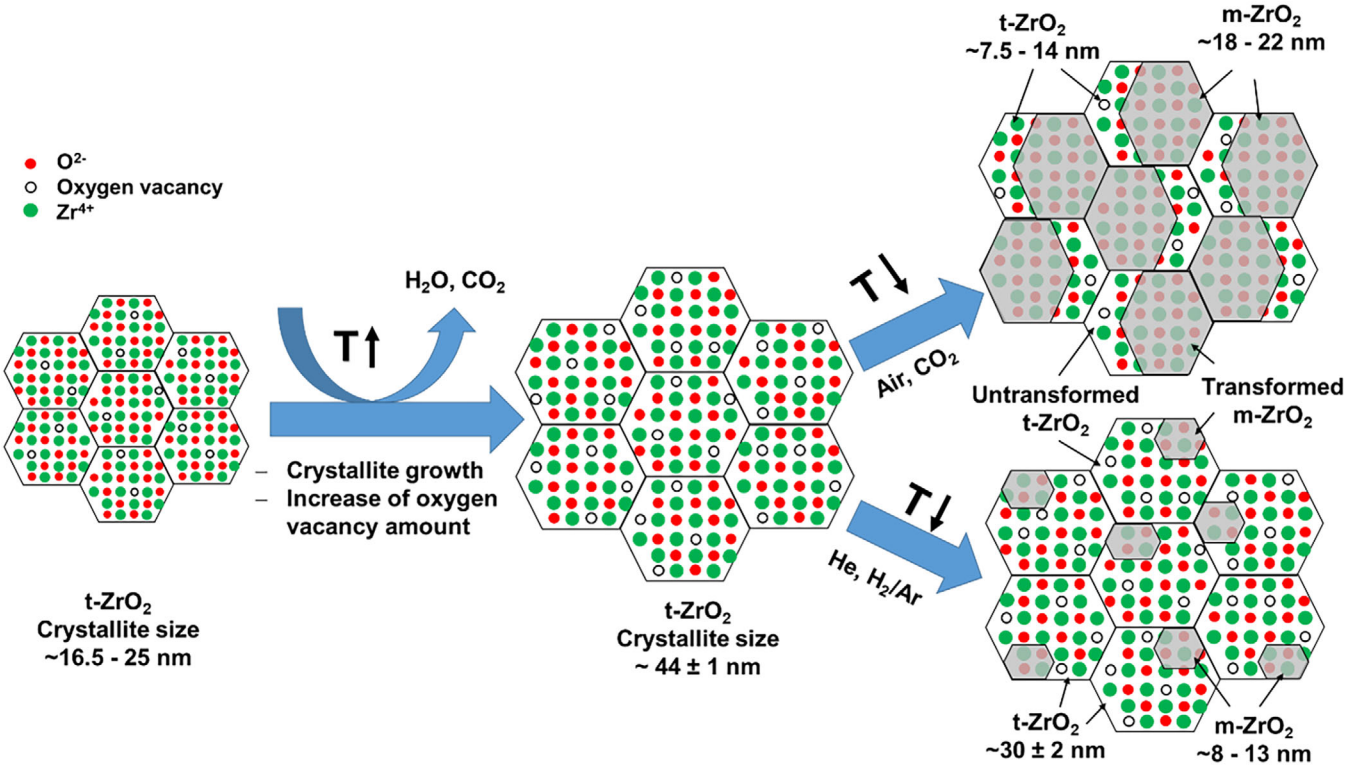

FIGURE 8 Schematic diagram for the possible transformation mechanisms of t-ZrO_2 into m-ZrO_2 showing the growth in the crystallite size and the increase in the oxygen vacancy concentration in t-ZrO_2 upon heating and formation of smaller m-ZrO_2 crystallites from within larger t-ZrO_2 particles upon cooling.

contrast, upon cooling in oxygen-free atmospheres (e.g., He and H_2/Ar), the unfilled oxygen vacancies stabilize the t-ZrO_2 phase, whereas m-ZrO_2 phase nucleates in the regions with lower oxygen vacancy concentration. Thus, the reduction of t-ZrO_2 during heating and subsequent stabilization of generated oxygen vacancies during cooling in the oxygen-free atmospheres (i.e., 5 vol% H_2/Ar and He) could stabilize t-ZrO_2 phase and lower the weight fraction of formed m-ZrO_2 (see Table 1). In contrast, refilling the generated oxygen vacancies on t-ZrO_2 phase during cooling in the oxygen-containing atmospheres (i.e., CO_2 and air) promotes the transformation of t-ZrO_2 into m-ZrO_2. From that perspective, our finding confirms previously proposed mechanisms for the t → m-ZrO_2 phase transformation.[45,46]

4 | CONCLUSIONS

By a complementary quantitative XRD and electron microscopy analysis, we have shown the influence of the reduction potential of the gas atmosphere on the phase transformations in t-ZrO_2 and m-ZrO_2. Inert and reductive environments stabilize metastable t-ZrO_2 polymorph relative to more oxidizing environments, directly affecting the structural and morphological properties of both polymorphs, including grain size, unit cell volume, weight fraction, and structural defects. The different pathway of phase transformation as a function of the gas atmosphere is directly revealed by the final grain sizes adopted by both t-ZrO_2 and m-ZrO_2 and the resulting kinetic limitations of grain sintering. The phase transformation of t-ZrO_2 to m-ZrO_2 is rather governed by the stability of the existing defects (e.g., as a result of the preparation pathway) and less by the introduction of further vacancies (by, e.g., reduction) but *strongly entangled* with particle size evolution. As a pre-step to grain size analysis, we have elaborated a proper concept of electron microscopy analysis, allowing us to provide reliable quantification results of particle/grain sizes in oxide composite mixtures. Especially for polymorphic mixtures, distinguishing the different individual grain sizes in larger agglomerates necessitates a sophisticated treatment of electron microscopic images, including a succession of Fourier and inverse Fourier filtering of HR images.

ACKNOWLEDGMENTS

We thank the FWF (Austrian Science Foundation) for financial support under project F4503-N16 of the SFB "Functional Oxide Surfaces and Interfaces" (FOXSI). This

work has been performed within the framework of the research platform "materials and nanoscience" and the doctoral college "reactivity and catalysis" at the University of Innsbruck. L. Schlicker appreciates the ALS for supporting his work with a doctoral fellowship. This work is part of the Cluster of Excellence "Unifying Concepts in Catalysis" coordinated by the Technische Universität Berlin. Financial support by the Deutsche Forschungsgemeinschaft (DFG) within the framework of the German Initiative of Excellence is gratefully acknowledged. The authors thank the Advanced Light Source, which is supported by the Director, Office of Science, Office of Basic Energy Sciences, of the US Department of Energy under Contract No. DE-AC02-05CH11231, and where the in situ XRD measurements were conducted at beamline 12.2.2 in the framework of the AP proposals (ALS-08408 and ALS-11921).

Open access funding enabled and organized by Projekt DEAL.

ORCID

Maged F. Bekheet https://orcid.org/0000-0003-1778-0288
Lukas Schlicker https://orcid.org/0000-0001-7054-7587
Radian Popescu https://orcid.org/0000-0002-4954-0716
Wiebke Riedel https://orcid.org/0000-0001-6561-2305
Simon Penner https://orcid.org/0000-0002-2561-5816
Aleksander Gurlo https://orcid.org/0000-0001-7047-666X

REFERENCES

1. Ploner K, Delir Kheyrollahi Nezhad P, Watschinger M, Schlicker L, Bekheet MF, Gurlo A, et al. Steering the methanol steam reforming performance of Cu/ZrO_2 catalysts by modification of the Cu-ZrO_2 interface dimensions resulting from Cu loading variation. Appl Catal, A. 2021;623:118279. https://doi.org/10.1016/j.apcata.2021.118279
2. Song X, Sayari A. Sulfated zirconia-based strong solid-acid catalysts: recent progress. Catal Rev. 1996;38:329–412. https://doi.org/10.1080/01614949608006462
3. Shukla S, Seal S. Mechanisms of room temperature metastable tetragonal phase stabilisation in zirconia. Int Mater Rev. 2005;50:45–64. https://doi.org/10.1179/174328005İ14267
4. Kouva S, Honkala K, Lefferts L, Kanervo J. Review: monoclinic zirconia, its surface sites and their interaction with carbon monoxide. Catal Sci Technol. 2015;5:3473–90. https://doi.org/10.1039/C5CY00330J
5. Han Y, Zhu J. Surface science studies on the zirconia-based model catalysts. Top Catal. (Topics in Catalysis). 2013;56:1525–41. https://doi.org/10.1007/s11244-013-0156-5
6. Novik NN, Konakov VG, ArchakovIvan IY. Zirconia and ceria based ceramics and nanoceramics—a review on electrochemical and mechanical properties. Rev Adv Mater Sci. 2015;40:188–207.
7. Panda D, Tseng T-Y. Growth, dielectric properties, and memory device applications of ZrO_2 thin films. Thin Solid Films. 2013;531:1–20. https://doi.org/10.1016/j.tsf.2013.01.004
8. Atkinson A, Barnett S, Gorte RJ, Irvine JTS, McEvoy AJ, Mogensen M, et al. Advanced anodes for high-temperature fuel cells. Nat Mater. 2004;3:17–27. https://doi.org/10.1038/nmat1040
9. Hannink RHJ, Kelly PM, Muddle BC. Transformation toughening in zirconia-containing ceramics. J Am Ceram Soc. 2000;83:461–87. https://doi.org/10.1111/j.1151-2916.2000.tb01221.x
10. Barnard AS, Yeredla RR, Xu H. Modelling the effect of particle shape on the phase stability of ZrO_2 nanoparticles. Nanotechnology. 2006;17:3039–47. https://doi.org/10.1088/0957-4484/17/12/038
11. Piskorz W, Gryboś J, Zasada F, Zapała P, Cristol S, Paul J-F, et al. Periodic DFT study of the tetragonal ZrO 2 nanocrystals: equilibrium morphology modeling and atomistic surface hydration thermodynamics. J Phys Chem C. 2012;116:19307–20. https://doi.org/10.1021/jp3050059
12. Jin X-J. Martensitic transformation in zirconia containing ceramics and its applications. Curr Opin Solid State Mater Sci. 2005;9:313–18. https://doi.org/10.1016/j.cossms.2006.02.012
13. Wu Y, Chen J, Hu W, Zhao K, Qu P, Shen P, et al. Phase transformation and oxygen vacancies in Pd/ZrO_2 for complete methane oxidation under lean conditions. J Catal. 2019;377:565–76. https://doi.org/10.1016/j.jcat.2019.04.047
14. Wang C-M, Fan K-N, Liu Z-P. Origin of oxide sensitivity in gold-based catalysts: a first principle study of CO oxidation over Au supported on monoclinic and tetragonal ZrO_2. J Am Chem Soc. 2007;129:2642–47. https://doi.org/10.1021/ja067510z
15. Haug L, Thurner C, Bekheet MF, Bischoff B, Gurlo A, Kunz M, et al. Zirconium carbide mediates coke-resistant methane dry reforming on nickel-zirconium catalysts. Angew Chem Int Ed Engl. 2022;61:e202213249. https://doi.org/10.1002/anie.202213249
16. Bansal G, Heuer A. On a martensitic phase transformation in zirconia (ZrO_2)—I. Metallographic evidence. Acta Metall. 1972;20:1281–89. https://doi.org/10.1016/0001-6160(72)90059-4
17. Mamivand M, Asle Zaeem M, El Kadiri H, Chen L-Q. Phase field modeling of the tetragonal-to-monoclinic phase transformation in zirconia. Acta Mater. 2013;61:5223–35. https://doi.org/10.1016/j.actamat.2013.05.015
18. Chevalier J, Gremillard L, Virkar AV, Clarke DR The tetragonal-monoclinic transformation in zirconia: lessons learned and future trends. J Am Ceram Soc. 2009;92:1901–20. https://doi.org/10.1111/j.1551-2916.2009.03278.x
19. Kelly PM, Ball CJ. Crystallography of stress-induced martensitic transformations in partially stabilized zirconia. J Am Ceram Soc. 1986;69:259–64. https://doi.org/10.1111/j.1151-2916.1986.tb07421.x
20. Muddle BC, Hannink RHJ. Crystallography of the tetragonal to monoclinic transformation in MgO-partially-stabilized zirconia. J Am Ceram Soc. 1986;69:547–55. https://doi.org/10.1111/j.1151-2916.1986.tb04791.x
21. Navruz N. A comparative crystallographic analysis of the tetragonal-to-monoclinic transformation in the yttria-zirconia system. Phys Metals Metallogr. 2008;105:580–85. https://doi.org/10.1134/S0031918İ08060082
22. Kelly PM, Francis Rose LR. The martensitic transformation in ceramics—its role in transformation toughening.

Prog Mater Sci. 2002;47:463–557. https://doi.org/10.1016/S0079-6425(00)00005-0
23. Oleshko VP, Howe JM, Shukla S, Seal S. High-resolution and analytical TEM investigation of metastable-tetragonal phase stabilization in undoped nanocrystalline zirconia. J Nanosci Nanotechnol. 2004;4:867–75. https://doi.org/10.1166/jnn.2004.110
24. Rühle M. Microscopy of structural ceramics microscopy of structural ceramics. Adv Mater. 1997;9:195–217. https://doi.org/10.1002/adma.19970090304
25. Shukla S, Seal S, Vij R, Bandyopadhyay S, Rahman Z. Effect of nanocrystallite morphology on the metastable tetragonal phase stabilization in zirconia. Nano Lett. 2002;2:989–93. https://doi.org/10.1021/nl025660b
26. Garvie RC. The occurrence of metastable tetragonal zirconia as a crystallite size effect. J Phys Chem. 1965;69:1238–43. https://doi.org/10.1021/j100888a024
27. Kriven WM, Fraser WL, Kennedy SW. Martensite crystallography of tetragonal zirconia. Advances in Ceramics. 1981;3:82–97.
28. Srinivasan R, Davis BH, Cavin OB, Hubbard CR. Crystallization and phase transformation process in zirconia: an in situ high-temperature X-ray diffraction study. J Am Ceram Soc. 1992;75:1217–22. https://doi.org/10.1111/j.1151-2916.1992.tb05560.x
29. Leib EW, Vainio U, Pasquarelli RM, Kus J, Czaschke C, Walter N, et al. Synthesis and thermal stability of zirconia and yttria-stabilized zirconia microspheres. J Colloid Interface Sci. 2015;448:582–92. https://doi.org/10.1016/j.jcis.2015.02.049
30. Kogler M, Köck E-M, Vanicek S, Schmidmair D, Götsch T, Stöger-Pollach M, et al. Enhanced kinetic stability of pure and Y-doped tetragonal ZrO_2. Inorg Chem. 2014;53:13247–57. https://doi.org/10.1021/ic502623t
31. Köck E-M, Kogler M, Götsch T, Schlicker L, Bekheet MF, Doran A, et al. Surface chemistry of pure tetragonal ZrO_2 and gas-phase dependence of the tetragonal-to-monoclinic ZrO_2 transformation. Dalton Trans. 2017;46:4554–70. https://doi.org/10.1039/C6DT04847A
32. Doran A, Schlicker L, Beavers CM, Bhat S, Bekheet MF, Gurlo A. Compact low power infrared tube furnace for in situ X-ray powder diffraction. Rev Sci Instrum. 2017;88:13903. https://doi.org/10.1063/1.4973561
33. Schlicker L, Doran A, Schneppmüller P, Gili A, Czasny M, Penner S, et al. Transmission in situ and operando high temperature X-ray powder diffraction in variable gaseous environments. Rev Sci Instrum. 2018;89:33904. https://doi.org/10.1063/1.5001695
34. Bekheet MF, Delir Kheyrollahi Nezhad P, Bonmassar N, Schlicker L, Gili A, Praetz S, et al. Steering the methane dry reforming reactivity of Ni/La_2O_3 catalysts by controlled in situ decomposition of doped La_2NiO_4 precursor structures. ACS Catal. 2021;11:43–59. https://doi.org/10.1021/acscatal.0c04290
35. Bekheet MF, Grünbacher M, Schlicker L, Gili A, Doran A, Epping JD, et al. On the structural stability of crystalline ceria phases in undoped and acceptor-doped ceria materials under in situ reduction conditions. CrystEngComm. 2019;21:145–54. https://doi.org/10.1039/c8ce01726c
36. Götsch T, Schlicker L, Bekheet MF, Doran A, Grünbacher M, Praty C, et al. Structural investigations of $La_{0.6}Sr_{0.4}FeO_{3-\delta}$ under reducing conditions: kinetic and thermodynamic limitations for phase transformations and iron exsolution phenomena. RSC Adv. 2018;8:3120–31. https://doi.org/10.1039/c7ra12309d
37. Bekheet MF, Miehe G, Fasel C, Gurlo A, Riedel R. Low temperature synthesis of nanocrystalline $MnIn_2O_4$ spinel. Dalton Trans. 2012;41:3374–76. https://doi.org/10.1039/C2DT12473D
38. Bekheet MF, Schlicker L, Doran A, Siemensmeyer K, Gurlo A. Ferrimagnetism in manganese-rich gallium and aluminium spinels due to mixed valence Mn^{2+}–Mn^{3+} states. Dalton Trans. 2018;47:2727–38. https://doi.org/10.1039/c7dt04765g
39. Matta J, Lamonier J-F, Abi-Aad E, Zhilinskaya EA, Aboukaïs A. Transformation of tetragonal zirconia phase to monoclinic phase in the presence of Fe^{3+} ions as probes: an EPR study. Phys Chem Chem Phys. 1999;1:4975–80. https://doi.org/10.1039/a904828f
40. Wimmer EJ, Klostermann SV, Ringenberg M, Kästner J, Estes DP. Oxo-bridged Zr Dimers as well-defined models of oxygen vacancies on ZrO 2. Eur J Inorg Chem. 2023;26:e202200709. https://doi.org/10.1002/ejic.202200709
41. Gionco C, Paganini MC, Giamello E, Burgess R, Di Valentin C, Pacchioni G. Paramagnetic defects in polycrystalline zirconia: an EPR and DFT study. Chem Mater. 2013;25:2243–53. https://doi.org/10.1021/cm400728j
42. Chary KVR, Sagar GV, Srikanth CS, Rao VV. Characterization and catalytic functionalities of copper oxide catalysts supported on zirconia. J Phys Chem B. 2007;111:543–50. https://doi.org/10.1021/jp063335x
43. Speight JG. Upgrading by gasification. In: Heavy oil recovery and upgrading. Amsterdam: Elsevier; 2019. p. 559–614.
44. Sinhamahapatra A, Jeon J-P, Kang J, Han B, Yu J-S. Oxygen-deficient zirconia (ZrO_{2-x}): a new material for solar light absorption. Sci Rep. 2016;6:27218. https://doi.org/10.1038/srep27218
45. Leib EW, Pasquarelli RM, Blankenburg M, Müller M, Schreyer A, Janssen R, et al. High-temperature stable zirconia particles doped with yttrium, lanthanum, and gadolinium. Part Part Syst Charact. 2016;33:645–55. https://doi.org/10.1002/ppsc.201600069
46. Kountouros P, Petzow G. Defect chemistry, phase stability and properties of zirconia polycrystals. Science and technology of zirconia V. 1st ed. Boca Raton: CRC Press; 1993.

SUPPORTING INFORMATION

Additional supporting information can be found online in the Supporting Information section at the end of this article.

How to cite this article: Bekheet MF, Schlicker L, Popescu R, Riedel W, Grünbacher M, Penner S, et al. A quantitative microscopic view on the gas-phase-dependent phase transformation from tetragonal to monoclinic ZrO_2. J Am Ceram Soc. 2024;107:5036–50. https://doi.org/10.1111/jace.19749